Synthesis and Physicochemical Properties of $Er_{0.5}Dy_{0.5}Ba_2Cu_3O_{6.83}$ Cuprate High-Temperature Superconductor

P. Pęczkowski[a,b,*], M. Kowalik[c], Z. Jaegermann[b], P. Szterner[b], P. Zachariasz[d]
and W.M. Woch[c]

[a]Cardinal Stefan Wyszyński University, Faculty of Mathematics and Natural Sciences. School of Exact Sciences,
Department of Physics, K. Wóycickiego 1/3, 01-938 Warsaw, Poland

[b]Institute of Ceramics and Building Materials, Department of Ceramic Technology,
Postępu 9, 02-676 Warsaw, Poland

[c]AGH University of Science and Technology, Faculty of Physics and Computer Science,
Department of Solid State Physics, al. A. Mickiewicza 30, 30-059 Cracow, Poland

[d]Institute of Electron Technology, Department of Microelectronics, Zabłocie 39, 30-701 Cracow, Poland

The aim of this research was an analysis of physicochemical properties of a ceramic high-temperature super-conductor $Er_{0.5}Dy_{0.5}Ba_2Cu_3O_{6.83}$. Qualitative and quantitative phase analysis of the raw material sintering and annealing in oxygen atmosphere was performed by method of X-ray diffraction. The structural analysis revealed that the high-temperature superconductors mainly crystalize in orthorhombic phase with small traces of $BaCuO_2$ and CuO. Local microstructure analysis was carried out by scanning electron microscopy. The thermogravimetric and differential thermal analysis show that in addition to the presence of the main phase, other phases are also observed. Critical temperatures T_{c0} and T_c, critical current density J_c and superconducting transition width ΔT were evaluated from resistance and AC susceptibility measurements.

1. Introduction

In a numerous group of superconductors, one can distinguish the low-temperature superconductors (LTS), where superconductivity state exists below 30 K, and the high-temperature superconductors (HTS) having critical temperature above 30 K. Over the last 30 years many materials belonging to the high-temperature superconductors group have been discovered [1–7]. They are of great interest because of their electrical and magnetic properties and their practical applicability [8–10].

So far, many studies have been focused on the properties of superconducting ceramic $YBa_2Cu_3O_{7-x}$ (YBCO). In recent years, many articles were published describing the properties of $REBa_2Cu_3O_{7-x}$, materials in which yttrium (Y) were replaced by other rare earth elements, in particular Er, Ho, Dy, Gd, Eu, Sm, Nd, La or their combinations [11–14]. Among other, the research is focused on the resistivity of these compounds in function of temperature [11] and the impact of high-pressure treatment on conductivity and critical temperature [15, 16].

In the article by Kumar-Naik et al. [17], the authors analyzed the structural properties of materials $REBa_2Cu_3O_{7-x}$ (RE = Gd, Sm, Nd in equal proportion) in function of the infiltration growth process.

Fetisov et al. [18] discussed the thermal and spectroscopic results of $DyBa_2Cu_3O_{7-x}$. The motivation of these studies was to analyse the results of Murugesan et al. [19] showing higher stability towards corrosion of $DyBa_2Cu_3O_{7-x}$ relative to $YBa_2Cu_3O_{7-x}$.

The physical properties of the ceramic superconductors mainly depend on the synthesis methods and the technological aspects used for preparing the raw materials [20–22]. A large effort is aimed for reducing the costs and time of producing a material with the relevant properties. In present study a superconducting material $Er_{0.5}Dy_{0.5}Ba_2Cu_3O_{7-x}$ was fabricated by a solid state reaction method and its physicochemical properties were compared with the reference $YBa_2Cu_3O_{7-x}$ sample [23, 24]. The Er and Dy atoms were selected due to the similarity of the effective ionic radii for Er^{3+} (89.0 pm) and Dy^{3+} (91.2 pm), whose average value 90.1 pm is close to that of Y^{3+} (90.0 pm) [24, 25].

2. Experimental

2.1. Synthesis procedure

For material synthesis, we used Sigma Aldrich substrates of erbium(III) oxide — Er_2O_3, dysprosium(III) oxide — Dy_2O_3 (both with 99.99% purity), POCH barium carbonate — $BaCO_3$ with purity of 99.6%, and Alfa Aesar copper(II) oxide — CuO with purity of 99.999%.

After weighing the substrates in an appropriate amounts the mixture of powders was milled with isopropanol in a ratio of 1:1. After drying, the powder was

---

*corresponding author; e-mail: p.peczkowski@wp.pl

twice sintered in order to perform a solid state reaction. After each sintering step, the sinter was ground in a mortar. The both sintering step were carried out in air atmosphere in an electric muffle furnace according to the temperature profile shown in Fig. 1.
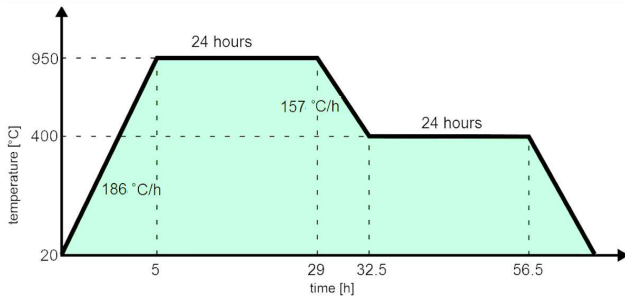

Fig. 1. Temperature profile of sintering steps for $REBa_2Cu_3O_{7-x}$.

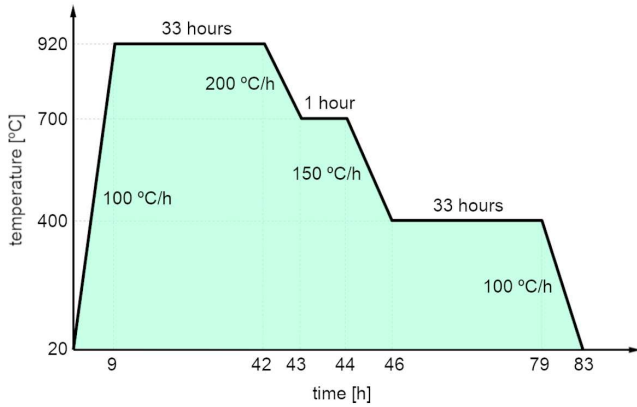Fig. 2. Temperature profile of annealing in oxygen atmosphere for $REBa_2Cu_3O_{7-x}$ [26].

The samples were formed into pellets of 12 mm in diameter and 1.5 mm thick by uniaxial pressing at 800 MPa. The annealing were made in the oxygen atmosphere (flow of 20 l/h) according to the temperature profile presented in Fig. 2.

2.2. Characterization

X-ray diffraction measurements of the sinters after the sintering and annealing steps were made by Brucker AXS D8 Discaver, where quantitative measurements were carried out by means of the Rietveld analysis in Topas software.

Sample morphology and local microstructure analysis were performed by using the FEI Nova NANOSEM 2000 field emission electron microscope equipped with the ETD (Everhart-Thornley detector).

The zero field cooling (ZFC) dispersion χ' and absorption χ'' parts of AC susceptibility were measured as a function of temperature and H_{AC} magnetic field amplitudes ranging from 0.022 Oe to 10.9 Oe by a standard mutual inductance bridge operating at the frequency of 189 Hz. A Stanford Research System SR830 DSP lock-in amplifier served both as a source for the AC current for the coil producing the AC magnetic field and as a voltmeter of the bridge. The applied magnetic field H_{AC} was parallel to the surface plane of the rectangular prism cut from the pellet. The temperature was monitored by the Lake Shore Model 330 autotuning temperature controller with chromel-gold — 0.07% Fe thermocouple of 0.3 K accuracy and resolution of 0.05 K. The above apparatus was also used in measurements of the resistance vs. temperature by the four-point method.

3. Results and discussion

The microscopic images of the milled raw powders show that the rare earth oxide grains (Er_2O_3, Dy_2O_3) have various shapes and are cracked, the barium carbonate ($BaCO_3$) grains are oriented in one direction, while the copper oxide (CuO) grains create highly porous agglomerates (Fig. 3).

The highest average apparent density were reached for $Er_{0.5}Dy_{0.5}Ba_2Cu_3O_{7-x}$ sample before annealing in oxygen atmosphere (6.31 ± 0.15) g/cm^3 and after annealing (5.62 ± 0.06) g/cm^3. For comparison, the average density of $YBa_2Cu_3O_{7-x}$ were (5.25 ± 0.09) g/cm^3 and (4.89 ± 0.06) g/cm^3 before and after annealing, respectively.

The local microstructures of all superconductors are similar. The SEM images show the presence of large grains and areas containing smaller, well-sintered grains.

Qualitative and quantitative powder phase analysis was performed with X-ray diffraction (XRD) method. Accuracy of the method was about 1%. In Tables I and II are presented the results of the crystalline phase content of the individual samples.

The X-ray analysis showed that after the second sintering, the amount of the superconducting phase $REBa_2Cu_3O_{7-x}$ was increased, while the contributions of $BaCuO_2$, $BaCO_3$, CuO, and RE_2BaCuO_5 were decreased. For $DyBa_2Cu_3O_{7-x}$ and $Er_{0.5}Dy_{0.5}Ba_2Cu_3O_{7-x}$ the $BaCO_3$ crystalline phase disappears after the second sintering (Table I).

The oxygen factor $x = 0.17$ in crystalline phase $REBa_2Cu_3O_{6.83}$ were calculated by Rietveld method based on published crystalline structures (COD and PDF + 2014, including ICSD).

The phase analysis after annealing in an oxygen atmosphere showed that the orthorhombic $REBa_2Cu_3O_{6.83}$ is a major phase, and only small contributions of $BaCuO_2$ and CuO were identified in the samples (Table II). SEM of the $REBa_2Cu_3O_{6.83}$ samples microstructure are shown in Fig. 4.

In the case of ideally mixed precursors only one-fold sintering should be sufficient to obtain single-phase $REBa_2Cu_3O_{7-x}$ sample. Nevertheless, in a real technological process the number of obtained crystalline phases depends on how well the precursors were mixed. As one can follow the results shown in Table I and
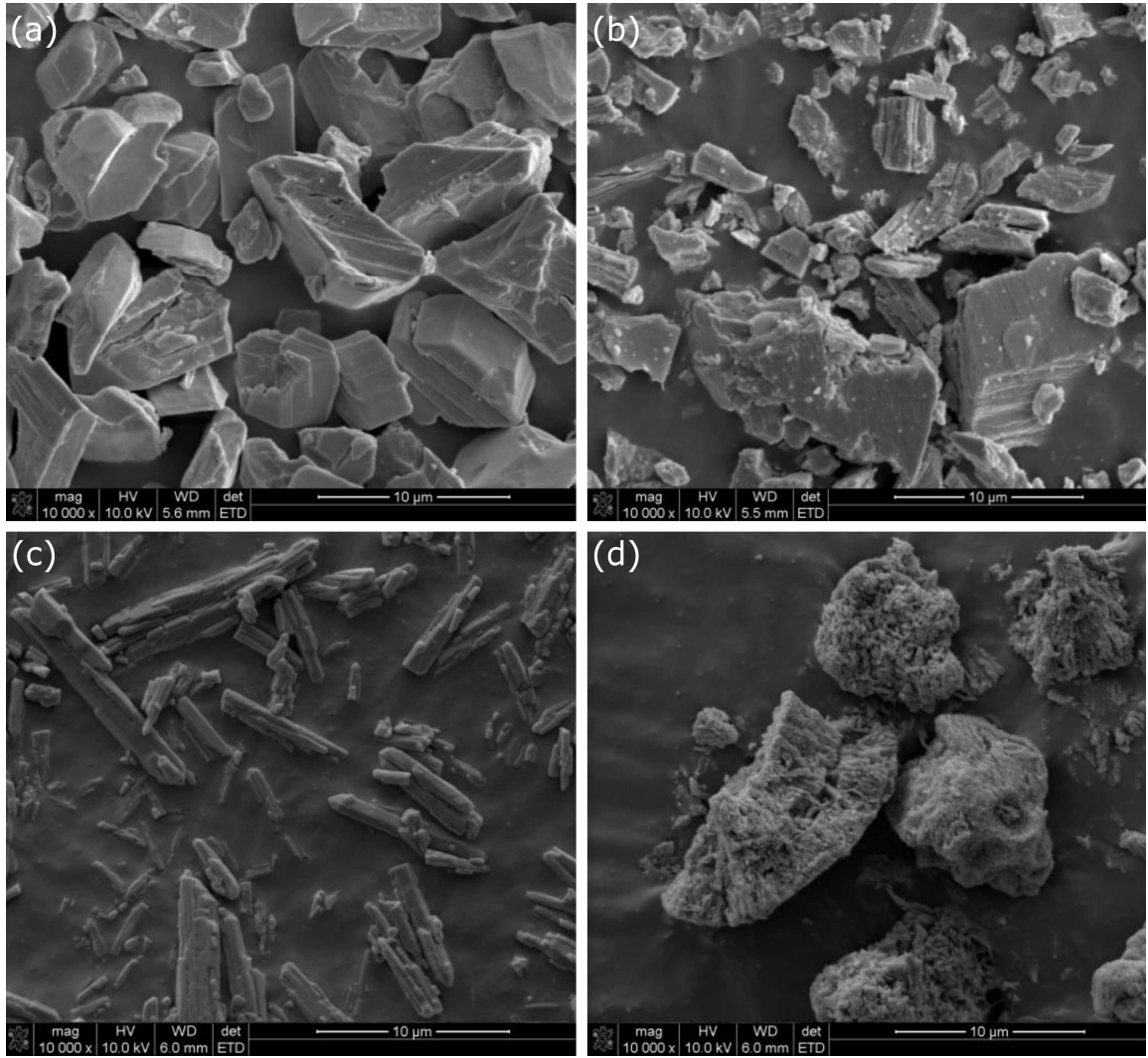
Fig. 3. SEM images of raw powders used for the preparation of REBCO with ETD detector (magnification: $10000\times$):
(a) Er_2O_3, (b) Dy_2O_3, (c) $BaCO_3$, (d) CuO.

TABLE I

Crystalline phase contents of $ErBa_2Cu_3O_{7-x}$, $DyBa_2Cu_3O_{7-x}$, $Er_{0.5}Dy_{0.5}Ba_2Cu_3O_{7-x}$, $YBa_2Cu_3O_{7-x}$ after first and second sintering

Crystalline phase	Phase content [wt. %]			
	$ErBa_2Cu_3O_{7-x}$	$DyBa_2Cu_3O_{7-x}$	$Er_{0.5}Dy_{0.5}Ba_2Cu_3O_{7-x}$	$YBa_2Cu_3O_{7-x}$
After first sintering				
$REBa_2Cu_3O_{7-x}$[a]	60.7 ± 0.7	72.2 ± 0.7	79.6 ± 0.5	70.7 ± 0.5
$BaCuO_2$	15.7 ± 0.3	4.9 ± 0.3	4.4 ± 0.2	8.1 ± 0.2
$BaCO_3$	3.9 ± 0.3	1.5 ± 0.3	2.6 ± 0.3	5.7 ± 0.2
CuO	9.6 ± 0.5	10.6 ± 0.4	5.4 ± 0.3	7.2 ± 0.3
RE_2BaCuO_5	10.1 ± 0.2	10.8 ± 0.2	8.0 ± 0.2	8.3 ± 0.2
After second sintering				
$REBa_2Cu_3O_{7-x}$[a]	74.7 ± 0.6	79.9 ± 0.7	89.5 ± 0.5	81.9 ± 0.6
$BaCuO_2$	7.6 ± 0.2	4.0 ± 0.3	3.0 ± 0.3	6.1 ± 0.3
$BaCO_3$	1.6 ± 0.2	$-$	$-$	2.9 ± 0.3
CuO	8.4 ± 0.3	10.5 ± 0.4	3.4 ± 0.3	4.1 ± 0.3
RE_2BaCuO_5	7.6 ± 0.2	5.5 ± 0.2	4.2 ± 0.2	4.9 ± 0.2

[a]RE = Er, Dy, $Er_{0.5}Dy_{0.5}$, Y

Results of Rietveld analysis of $ErBa_2Cu_3O_{6.83}$, $DyBa_2Cu_3O_{6.83}$, $Er_{0.5}Dy_{0.5}Ba_2Cu_3O_{6.83}$, $YBa_2Cu_3O_{6.83}$, samples after annealing in oxygen atmosphere

Crystalline phase	Phase content [wt. %]			
	$ErBa_2Cu_3O_{6.83}$	$DyBa_2Cu_3O_{6.83}$	$Er_{0.5}Dy_{0.5}Ba_2Cu_3O_{6.83}$	$YBa_2Cu_3O_{6.83}$
$REBa_2Cu_3O_{6.83}$[a]	91.3 ± 0.8	92.1 ± 0.7	98.1 ± 0.5	92.4 ± 0.5
$BaCuO_2$	3.3 ± 0.3	3.8 ± 0.2	0.9 ± 0.1	5.1 ± 0.2
CuO	5.5 ± 0.3	4.1 ± 0.4	1.0 ± 0.2	2.4 ± 0.2

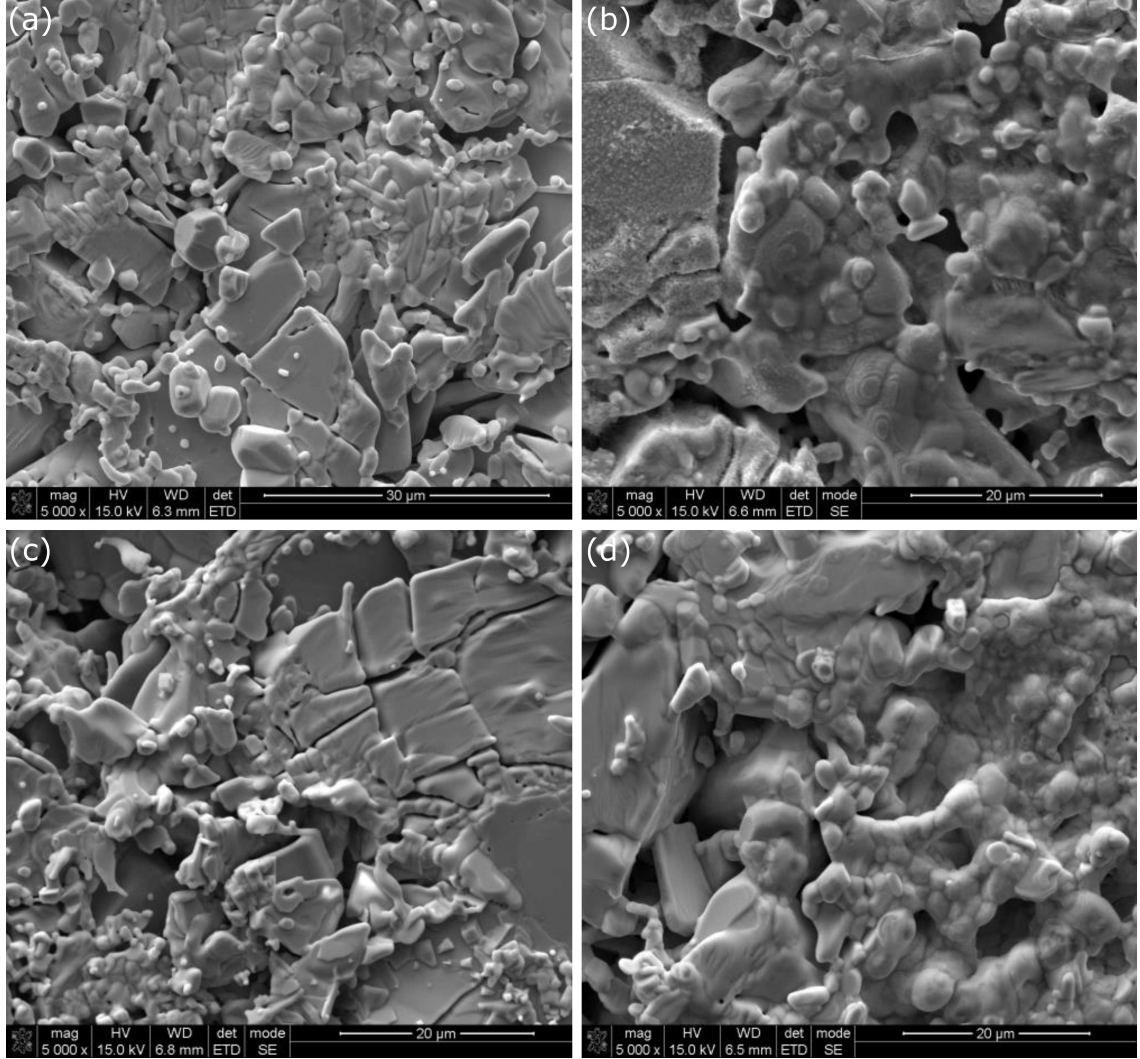[a]$RE = Er$, Dy, $Er_{0.5}Dy_{0.5}$, Y

Fig. 4. SEM images of $REBa_2Cu_3O_{6.83}$ microstructure with ETD detector (magnification: 5000x): (a) $Er_{0.5}Dy_{0.5}Ba_2Cu_3O_{6.83}$, (b) $ErBa_2Cu_3O_{7-x}$, (c) $DyBa_2Cu_3O_{6.83}$, (d) $YBa_2Cu_3O_{6.83}$.

Table II, the percentage quantity of superconducting crystalline phase $REBa_2Cu_3O_{7-x}$ increases with increasing number of the steps of milling followed by high-temperature annealing. The quantity of non-superconducting crystalline phases decreases. The extra mixing/grinding steps allow the minor phases to take part in solid state reaction, which results in creation of more superconducting crystalline phase $REBa_2Cu_3O_{7-x}$. $Er_{0.5}Dy_{0.5}Ba_2Cu_3O_{6.83}$ (0.9 ± 0.1) wt% but lower than for

After annealing in oxygen atmosphere, the highest amount of superconducting phase $REBa_2Cu_3O_{6.83}$ was found to be (98.1 ± 0.5) wt% in the mixed $Er_{0.5}Dy_{0.5}Ba_2Cu_3O_{6.83}$ sample, and the smallest amount of (91.3 ± 0.8) wt% in sample $ErBa_2Cu_3O_{6.83}$. The $BaCuO_2$ content of about ($3.3 \div 3.8$) wt% in the $ErBa_2Cu_3O_{6.83}$ and $DyBa_2Cu_3O_{6.83}$ ceramics is significantly higher than that for the mixed sample $YBa_2Cu_3O_{6.83}$ (5.1 ± 0.2) wt%. Also, CuO contributions
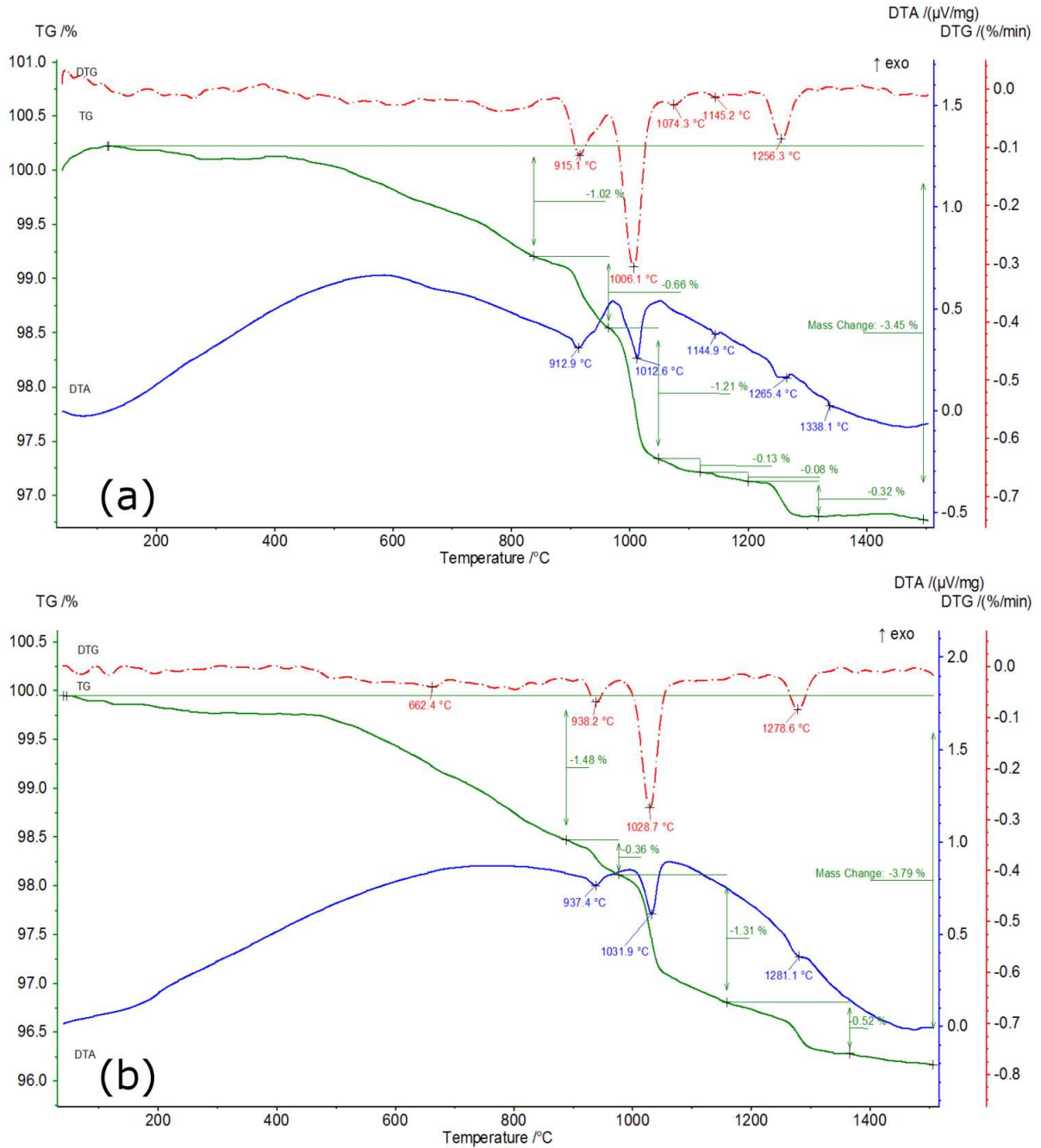
Fig. 5.   The TG/DTA for $Er_{0.5}Dy_{0.5}Ba_2Cu_3O_{7-x}$: (a) in air atmosphere after the first sintering, (b) in oxygen atmosphere after the second sintering.

in $ErBa_2Cu_3O_{6.83}$ (5.5 ± 0.3) wt% and $DyBa_2Cu_3O_{6.83}$ (4.1 ± 0.4) wt% are significantly higher than for the mixed sample $Er_{0.5}Dy_{0.5}Ba_2Cu_3O_{6.83}$ (1.0 ± 0.2) wt%.

The unit cell parameters for orthorhombic phase $REBa_2Cu_3O_{6.83}$ were determined by the Rietveld analysis of the XRD patterns (Table III).

The unit cell parameters for orthorhombic phase $YBa_2Cu_3O_{6.83}$ are very similar to the parameters of $Er_{0.5}Dy_{0.5}Ba_2Cu_3O_{6.83}$. The volume of the unit cell for orthorhombic phase depends on the radius

TABLE III

The unit cell parameters for orthorhombic phase $REBa_2Cu_3O_{6.83}$

Superconductor	a [nm]	b [nm]	c [nm]	V [nm³]	ρ [g/cm³]
$ErBa_2Cu_3O_{6.83}$	0.3826	0.3880	1.1671	0.1733	7.123
$DyBa_2Cu_3O_{6.83}$	0.3850	0.3878	1.1682	0.1744	7.030
$Er_{0.5}Dy_{0.5}Ba_2Cu_3O_{6.83}$	0.3830	0.3884	1.1674	0.1737	7.084
$YBa_2Cu_3O_{6.83}$	0.3831	0.3882	1.1675	0.1736	6.350

of the RE^{3+} ion. The mean radius of the ions Er^{3+} and Dy^{3+} is similar to the radius of the Y^{3+}, therefore the unit cell volumes for orthorhombic phase are comparable [24, 25].

Since the main purpose of this work was to characterize the superconductor $Er_{0.5}Dy_{0.5}Ba_2Cu_3O_{7-x}$, the results of thermal and magnetic investigations of this material were only included in the article.

The results of the thermogravimetric–differential thermal analysis (TG–DTA) carried out in air atmosphere after the first and second sintering for $Er_{0.5}Dy_{0.5}Ba_2Cu_3O_{7-x}$ are shown in Fig. 5. One can see the characteristic temperatures of endothermic reactions, where a formation of $Er_{0.5}Dy_{0.5}Ba_2Cu_3O_{7-x}$ phase take place around 912.9 °C and about 937.4 °C after the first and the second sintering, respectively. On the other hand, the peritectic reactions associated with the decomposition of $Er_{0.5}Dy_{0.5}Ba_2Cu_2O_{7-x}$ to $Er_{0.5}Dy_{0.5}Ba_2Cu_2O_5$, $Ba_2Cu_2O_5$ and $BaCuO_2$ are characteristic around 1012.6 °C and 1031.9 °C after the first and second sintering. Also, the thermograms show that, in addition to the main $Er_{0.5}Dy_{0.5}Ba_2Cu_2O_5$ phase, the other phases contribution to the additional effects are observed on the DTA curves [27, 28].
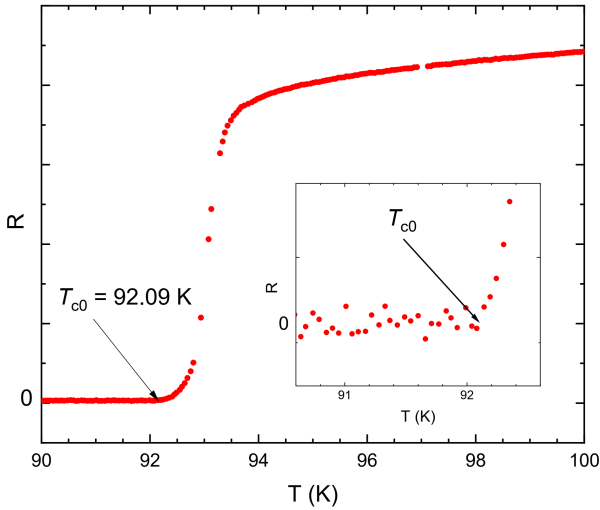

Fig. 6. Temperature dependence of the resistance of $Er_{0.5}Dy_{0.5}Ba_2Cu_3O_{6.83}$.

The temperature dependence of the resistance of $Er_{0.5}Dy_{0.5}Ba_2Cu_3O_{6.83}$ is shown in Fig. 6. The sample exhibits critical temperature $T_{c0} = (92.09 \pm 0.30)$ K and narrow superconducting transition $\Delta T = (0.69 \pm 0.05)$ K. The definitions of T_{c0} and ΔT are as in [29]. For comparison, the $DyBa_2Cu_3O_{6.83}$ sample studied in [30] has the critical temperature $T_c = (91.40 \pm 0.10)$ K and $\Delta T = (0.70 \pm 0.10)$ K. Moreover, the round-shaped $Er_{0.5}Dy_{0.5}Ba_2Cu_3O_{6.83}$ pellet of thickness 3 mm and 12 mm in diameter exhibits a specific resistance about (3.30 ± 0.15) mΩ cm, which was determined at room temperature using the van der Pauw method [31, 32].
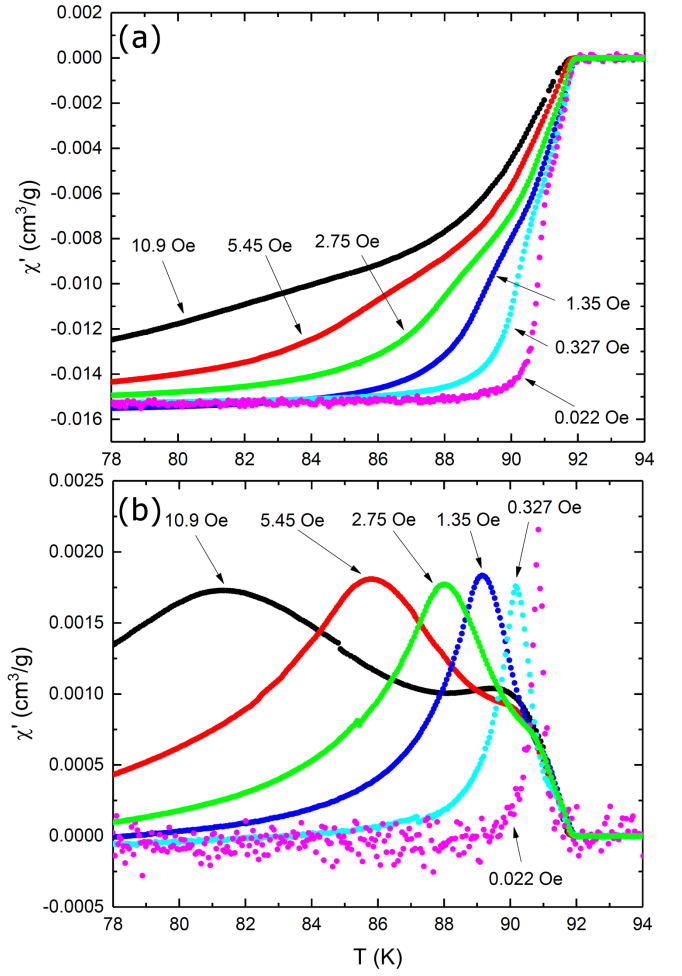

Fig. 7. The real (a) and imaginary (b) parts of the AC susceptibility for $Er_{0.5}Dy_{0.5}Ba_2Cu_3O_{6.83}$ in function of temperature and applied magnetic field.

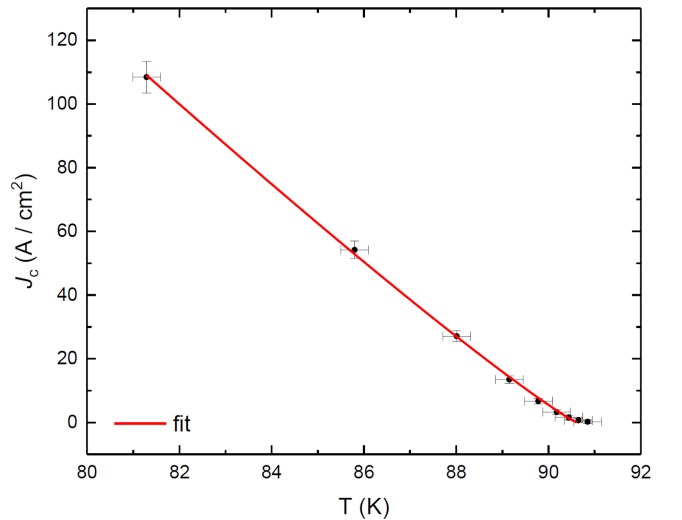
Fig. 8. The critical current density vs. temperature for $Er_{0.5}Dy_{0.5}Ba_2Cu_3O_{6.83}$ calculated from the Bean critical state model (Eq. (1)). The solid line is the fit to Eq. (2).

The ZFC dispersion χ' and absorption χ'' parts of AC susceptibility are show in Fig. 7. The intra-grain critical temperature $T_c = (92.10 \pm 0.30)$ K was determined from the dispersion part of AC susceptibility. The T_c was defined as the temperature corresponding to the last negative value of χ' when the temperature of the sample was increasing. The temperature dependences of the absorption part of AC susceptibility at different magnetic fields H_{AC} were measured in order to evaluate the critical current density J_c. In general, the absorption part of the AC susceptibility exhibits one peak associated with the energy losses related to the magnetic field penetration at grain boundary regions. In the case of the studied sample the absorption peak associated with the energy losses in grains was also observed. The former peak is located at lower temperatures than the latter. When the applied magnetic field H_{AC} is being increased, the intergrain peak moves faster to the lower temperatures than the intra-grain peak. According to the Bean critical state model the position of the absorption peak on the temperature axis is related to the critical current density J_c with formula (1) [33, 34]:

$$J_c = 2H_{AC}/d, \qquad (1)$$

where H_{AC} is the AC field amplitude and d is the sample thickness in the direction perpendicular to the magnetic field H_{AC}. The critical current flows through the grains and inter-grain regions. The critical current density is limited by the weakest junctions (i.e. intergrain regions) on the percolation path of the current. The calculated intergrain critical current densities J_c are presented in Fig. 8. According to the Ginzburg–Landau strong coupling limit approach, the critical current density varies with temperature according to the following equation [35]:

$$J_c = J_{c0}(1 - T/T_{cJ})^n, \qquad (2)$$

where T_{cJ} is the critical temperature of intergrain regions and J_{c0} is the intergrain critical current density at 0 K.

Figure 8 shows the temperature dependence of the critical current density fitted by Eq. (2), where the T_{cJ}, J_{c0} and n are fit parameters. The value of critical current density J_c at 77 K is about (165 ± 30) A cm^{-2} and is typical for bulk RE-123 HTS samples (where RE rare-earth element) with large grains and weak intergrain links. The values of fitted parameters are $T_{cJ} = (90.61 \pm 0.12)$ K, $J_{c0} = (1318 \pm 171)$ A cm^{-2} and $n = 1.096 \pm 0.056$.

4. Conclusion

The article describes a method of preparing the ceramic high-temperature superconductors based on the rare-earth elements RE = Er, Dy, Y. The materials were obtained by solid state reaction method followed by grinding, sintering, and annealing of the mixture of powders in oxygen atmosphere at high-temperature. Structural studies have confirmed that the orthorhombic phase is responsible for high-temperature superconductivity, and the $Er_{0.5}Dy_{0.5}Ba_2Cu_3O_{6.83}$ sample contains of about 98% of the superconducting phase.

Critical temperatures T_{c0} and T_c, critical current density J_c and superconducting transition width ΔT of $Er_{0.5}Dy_{0.5}Ba_2Cu_3O_{6.83}$ were evaluated from resistance and AC susceptibility vs. temperature measurements. The values of critical temperatures were $T_c = (92.10 \pm 0.30)$ K and $\Delta T = (0.70 \pm 0.10)$ K, $T_{c0} = (92.09 \pm 0.30)$ K and $\Delta T = (0.70 \pm 0.10)$ K. Critical current density $J_c = (165 \pm 30)$ A cm^{-2} at liquid nitrogen temperature was calculated using the Bean critical state model and the Ginzburg–Landau strong coupling limit approach.

References

[1] M.K. Wu, J.R. Ashburn, C.J. Torng, P.H. Hor, R.L. Meng, L. Gao, Z.J. Huang, Y.Q. Wang, C.W. Chu, *Phys. Rev. Lett.* **58**, 908 (1987).

[2] H. Maeda, Y. Tanaka, M. Fukutomi, T. Asano, *Jpn. J. Appl. Phys.* **27**, L209 (1988).

[3] Z.Z. Sheng, A.M. Hermann, *Nature* **332**, 55 (1988).

[4] J. Karpinski, E. Kaldis, E. Jilek, S. Rusiecki, B. Bucher, *Nature* **336**, 660 (1988).

[5] S.N. Putilin, E.V. Antipov, O. Chmaissem, M. Marezio, *Nature* **362**, 226 (1993).

[6] T. Kawashima, Y. Matsui, E. Takayama-Muromachi, *Physica C* **224**, 69 (1994).

[7] J. Schwartz, K.M. Amm, Y.R. Sun, C. Wolters, *Physica B* **216**, 261 (1996).

[8] C.W. Chu, P.H. Hor, R.L. Meng, L. Gao, Z.J. Huang, Y.Q. Wang, *Phys. Rev. Lett.* **58**, 911 (1987).

[9] P. Paturi, J. Raittila, J.C. Grivel, H. Huhtinen, B. Seifi, R. Laiho, N.H. Andersen, *Physica C* **372–376**, 779 (2002).

[10] K. Onabe, T. Doi, N. Kashima, S. Nagaya, T. Saitoh, *Physica C* **378–381**, 907 (2002).

[11] H.C. Yang, M.H. Hsieh, H.H. Sung, C.H. Chen, H.E. Horng, Y.S. Kan, H.C. Chen, J.C. Jao, *Phys. Rev. B* **39**, 9203 (1989).

[12] S.J. Jin, R.A. Fastnacht, T.H. Tiefel, R.C. Sherwood, *Phys. Rev. B* **37**, 5828 (1988).

[13] A. Salinas-Sanchez, J.L. Garcia-Muñoz, J. Rodriguez-Carvajal, R. Saez-Puche, J.L. Martinez, *J. Solid State Chem.* **100**, 201 (1992).

[14] P. Pęczkowski, M. Kowalik, P. Zachariasz, C. Jastrzębski, Z. Jaegermann, P. Szterner, W.M. Woch, J. Szczytko, *Phys. Status Solidi A* **215**, 1700888 (2018).

[15] K. Al-Shibani, A. Al-Aql, A. Al-Muezzin, H. Humeida, E.P. Nakhmedov, T. Firat, O. Öztürk, Ö.A. Sacli, *Phys. Status Solidi B* **189**, 177 (1995).

[16] P. Pęczkowski, P. Szterner, Z. Jaegermann, M. Kowalik, R. Zalecki, W.M. Woch, *J. Supercond. Nov. Magn.* **31**, 2719 (2018).

[17] S.P. Kumar-Naik, V.S. Bai, *Cryogenics* **81**, 47 (2017).

[18] A.V. Fetisov, G.A. Kozhina, S.K. Estemirova, V.B. Fetisov, R.I. Gulyaeva, *Physica C* **508**, 62 (2015).

[19] M. Murugesan, H. Obara, Y. Nakagawa, H. Yamasaki, Y. Mawatari, S. Kosaka, *Appl. Phys. Lett.* **88**, 252509 (2006).

[20] P. Pęczkowski, P. Szterner, Z. Jaegermann, *Sci. Works Instit. Ceram. Build. Mater.* **27**, 57 (2016).

[21] P. Szterner, P. Pęczkowski, Z. Jaegermann, *Sci. Works Instit. Ceram. Build. Mater.* **28**, 62 (2017).

[22] P. Szterner, P. Pęczkowski, Z. Jaegermann, *Sci. Works Instit. Ceram. Build. Mater.* **29**, 48, 61 (2017).

[23] M.K. Wu, J.R. Ashburn, C.J. Torng, P.H. Hor, R.L. Meng, L. Gao, Z.J. Huang, Y.Q. Wang, C.W. Chu, *Phys. Rev. Lett.* **58**, 908 (1987).

[24] C. Andreouli, A. Tsetsekou, *J. Eur. Ceramic. Soc.* **20**, 2101 (2000).

[25] Y. Xu, W. Guan, *Physica C* **212**, 119 (1993).

[26] S. Alagöz, *Tur. J. Phys.* **33**, 69 (2009).

[27] J. Plewa, H. Altenburg, J. Hauck, *Therm. Acta* **255**, 177 (1995).

[28] R. Redac, M. Zaharescu, *J. Therm. Anal. Calor.* **66**, 513 (2001).

[29] W.M. Woch, R. Zalecki, A. Kołodziejczyk, O. Heiml, G. Gritzner, *Physica C* **434**, 17 (2006).

[30] A. Kołodziejczyk, A. Kozłowski, J. Chmist, R. Zalecki, T. Ściężor, Z. Tarnawski, W.M. Woch, *Acta Phys. Pol. A* **84**, 127 (1993).

[31] L.J. Van der Pauw, *Philips Tech. Rev.* **20**, 220 (1958).

[32] L.J. Van der Pauw, *Philips Res. Rep.* **13**, 1 (1958).

[33] C.P. Bean, *Phys. Rev. Lett.* **8**, 250 (1962).

[34] J.R. Clem, *Physica C* **153**–**155**, 50 (1988).

[35] J.R. Clem, B. Bumble, S.I. Raider, W.J. Gallagher, Y.C. Shih, *Phys. Rev. B* **35**, 6637 (1987).